RSC Advances

PAPER

View Article Online
View Journal | View Issue

Cite this: *RSC Adv.*, 2020, **10**, 5108

The effects of the crosslinking position and degree of conjugation in perylene tetraanhydride bisimide microporous polymers on fluorescence sensing performance†

Chen Hu, Ying-Chun Gao, Can Zhang, Min Liu and Tong-Mou Geng *

Received 11th December 2019
Accepted 9th January 2020

DOI: 10.1039/c9ra10384h

rsc.li/rsc-advances

In this study, two fluorescence conjugated microporous polymers based on perylene tetraanhydride bisimide (DP_4A_0 and DP_4A_2) were prepared *via* Sonogashira–Hagihara cross-coupling polymerization for the efficient detection of *o*-nitrophenol (*o*-NP). They were well characterized *via* FT-IR, solid state ^{13}C NMR, elemental analysis, and other material characterization techniques. The experiments proved that both CMPs possess high thermal and chemical stability and a porous nature with Brunauer–Emmett–Teller (BET) specific surface areas of 41.3 and 402.1 $m^2\ g^{-1}$. Importantly, owing to signal amplification by the conjugated skeleton, DP_4A_0 and DP_4A_2 exhibit extremely high sensitivity to *o*-NP with K_{sv} values of 1.83×10^4 and 1.69×10^4 L mol^{-1} and limits of detection of 5.73×10^{-9} and 7.36×10^{-9} mol L^{-1}, respectively. The sensing performance of DP_4A_0 and DP_4A_2 was dependent on the position of crosslinking points and crosslinking density. Finally, super amplified quenching was considered the electron transfer mechanism and hydrogen bond interactions were also present.

Introduction

The determination of nitroaromatic compounds (NACs) has increased rapidly over the years because of its significance in environment, national defense, and public safety.[1–6] There are some techniques and devices used for detecting NACs, such as metal detectors, trained canines, gas chromatography coupled with mass spectrometry (GC-MS),[7] electrochemical methods,[8,9] ion mobility spectroscopy (IMS),[10] high performance liquid chromatography,[11] quartz crystal microbalance (QCM), colorimetry, and surface enhanced Raman spectroscopy (SERS).[6,12] Fluorescence detection methods have emerged as one of the most promising approaches because of the quick response time, moderate price, high sensitivity and selectivity, simple operation, and portability for on-site testing.[4,6] Although traditional fluorescent substances (such as organic fluorescent dyes) have made some progress, they have low limits of detection (LODs) and may result in more environmental pollution due to their toxicity, poor biodegradability, presence of redundant heavy metals as well as inferior chemical stability and photobleaching.[6] Because of the "aggregation-induced quenching (ACQ)" effects, most organic dyes deplete their excitation energy in their aggregated state. By covalently incorporating dye-based monomers into conjugated microporous polymers (CMPs), fluorophores can be separated spatially through porosity, thereby remarkably increasing the fluorescent intensity of the monomers, which are initially affected by ACQ.[13,14]

CMPs are worth the consideration for a variety of reasons: first, compared with similar building blocks, CMPs become prominent electron donors due to the expansion of π-conjugation. Furthermore, in virtue of the π* delocalization, the enhanced donating ability of CMPs in the excited state provides a platform for the facile migration of excitation. Therefore, the interaction between CMPs and NACs will augment and the fluorescence will be quenched, which is found by Swager *et al.*, known as 'molecular wire effect'.[15] The extended π-conjugation of conjugated polymers was shown to be an up-and-coming feature of amplified signal transduction.[3,16] Second, because they are constructed by carbon–carbon or carbon–nitrogen bonds, CMPs are thermally and chemically stable.[3,17] Third, the structure and porosity of the CMPs may be adjusted by judiciously selecting building blocks, since high porosity can enhance the rapid diffusion of NACs in porous frameworks and impactful host–guest interactions, leading to improved fluorescence quenching efficiency and sensitivity.[3]

Since the discovery of the first CMP in 2007,[18] there has been much interest in the synthesis and possible applications of these materials.[17,19,20] Numerous CMPs have been successfully synthesized and applied as chemosensors, particularly fluorescent CMPs, which have been employed for the detection of

AnHui Province Key Laboratory of Optoelectronic and Magnetism Functional Materials, School of Chemistry and Chemical Engineering, Anqing Normal University, Anqing 246011, China. E-mail: gengtongmou@aqnu.edu.cn

† Electronic supplementary information (ESI) available: Synthesis of DP_4A_0, DP_4A_2, solid UV-vis spectra, XRD, SEM, fluorescence spectra, Stern–Volmer plots, HOMO and LUMO values. See DOI: 10.1039/c9ra10384h

NACs.[21,22] NACs have strong electron acceptance ability. Therefore, adding NACs will affect the excited states of CMPs, which leads to fluorescence quenching.[23] Recently, we developed a fluorescent CMP based on perylene tetraanhydride bisimide (DP_2A_2) *via* a Sonogashira–Hagihara cross-coupling polymerization for sensing *o*-nitrophenol (*o*-NP).[14] In a continuation of our previous study, this paper reports the synthesis of two CMPs (DP_4A_0 and DP_4A_2) with high surface areas and microporosity (Scheme 1). The effects of different cross-linking points and densities on the fluorescence sensing properties of the CMPs were studied.

According to the serial numbers in Scheme 2, the cross-linking points of DP_4A_0 should be located at 1, 6, 7, and 12. The cross-linking points of DP_4A_2 should be located at 1, 6, 7, 12, 13, and 14 and the cross-linking points of DP_2A_2 should be located at 1, 7, 13, and 14.

Experimental section

Materials

Perylene-3,4:9,10-tetracarboxylic dianhydride (PTCDA, 98%), copper(I) iodide (CuI) (99.5%), 1,4-diethynylbenzene (DEB), and tetrakis(-triphenylphosphine) palladium ($Pd(PPh_3)_4$) were bought from Aladdin Chemistry Co. Ltd. *p*-Bromoaniline (99%) was purchased from J & K scientific Ltd. Bromine, 1,4-dioxane (DOX), acetonitrile (ACN), methanol, *N*,*N*-dimethylformamide (DMF, 99.0%), chloroform, ethanol (EtOH), tetrahydrofuran (THF) sodium hydrate, acetone, toluene, hydrochloric acid, diisopropylamine (DIA), *o*-NP, 4-nitrotoluene (*p*-NT), picric acid (PA), phenol (PhOH), dinitrotoluene (DNT), 1,3-dinitrobenzene (*m*-DNB), and 1,4-dinitrobenzene (*p*-DNB) were purchased commercially and used without further purification. *N*,*N*-Diphenyl-1,4,7,12-tetrabromoperylene-3,4:9,10-tetracarboxydiimide (PBr_4ABr_0) and *N*,*N*′-di(4-bromophenyl)-1,6,7,12-tetrabromoperylene-3,4:9,10-tetracarboxydiimide (PBr_4ABr_2) were synthesized in accordance with previous reports.[23,24]

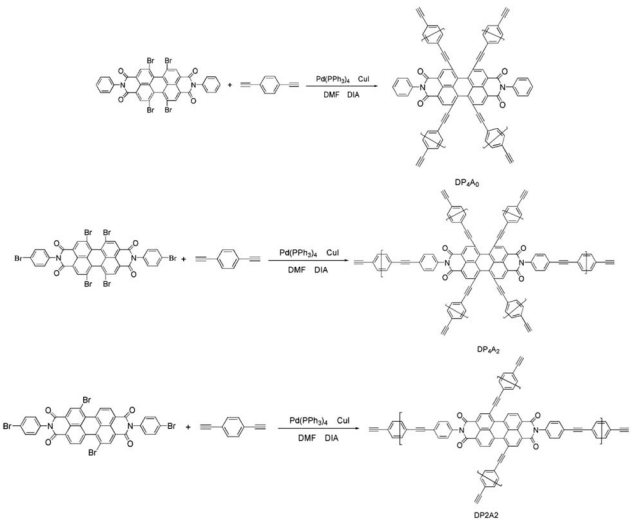

Scheme 1 Synthesis of DP_4A_0, DP_4A_2, and DP_2A_2 *via* Sonogashira–Hagihara cross-coupling reactions.

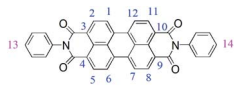

Scheme 2 The serial numbers of *N*,*N*′-diphenyl-perylene-3,4:9,10-tetracarboxydiimide.

Characterization, morphology analysis and methods

Fourier transform infrared (FT-IR) spectra were recorded on a Thermo Nicolet Nexus 8700 Fourier transform infrared spectrometer in KBr pellets. Solid-state ^{13}C cross polarization magic angle spinning NMR (ss ^{13}C NMR) spectra were recorded on a Bruker Avance III 400 NMR spectrometer, using a contact time of 2.0 ms and a relaxation delay of 10.0 s. Elemental analysis (EA) was performed on an analyzer (model VarioELIII). Solid UV-Vis absorption spectra were recorded using a PerkinElmer Lambda 950 UV-Vis spectrophotometer.

The thermal gravimetric analysis (TGA) measurements were performed using a Mettler ATA409PC thermo-gravimetric analysis instrument between room temperature to 800 °C at a heating rate of 10 °C min^{-1} under a N_2 atmosphere. Powder X-ray diffraction (PXRD) was examined on a Rigaku model XRD600 diffractometer equipped with Ni-filtered Cu Kα radiation (40 kV, 100 mA) by depositing powder on glass substrates at room temperature. The scanning speed was 5° min^{-1} and scanning ranges are from $2\theta = 5°$ to 60° with 0.02° increments. Scanning electron microscopy (SEM) was performed on a JEOL-3400LV and S-3400N microscope (Japan) with an accelerating voltage of 5.0 kV.

The specific surface area and pore size distributions were measured using a Bel Japan Inc. model BELSORP-mini II sorption analyzer with N_2 adsorption and desorption at 77 K, and the pore parameters (BET specific surface area, pore size, and pore volume) could be estimated from the adsorption–desorption isotherms. Samples were degassed at 150 °C in a vacuum for 10 h before each measurement. Fluorescence spectra were recorded at room temperature using Hitachi F-4500 spectrophotometers. A 0.1 mol L^{-1} THF–NACs stock solution was prepared. A 1.0 mg mL^{-1} solution of the dispersion colloid was obtained by adding DP_4A_0 or DP_4A_2 (25 mg) to THF (25 mL), followed by ultrasonic dispersion. As soon as the NAC solution was added, the fluorescence intensity of the dispersion was determined. The LODs were obtained using the equation: $LOD = 3s/\rho$, where s is the standard deviation of the blank measurement and ρ is the slope of the relative fluorescence intensity (I_0/I) over the sample concentration.

Results and discussion

DP_4A_0 and DP_4A_2 as well as their corresponding building blocks were prepared by following approaches found in previous reports.[14,24,25] The structures of DP_4A_0 and DP_4A_2 were confirmed *via* FT-IR spectroscopy, ss ^{13}C NMR spectroscopy, elemental analysis (EA), and UV-Vis absorption spectroscopy. The FT-IR spectra of both DP_4A_0 and DP_4A_2 (Fig. 1) showed peaks at 2189 and 2200 cm^{-1}, which are the characteristic of

bis-substituted acetylenes.[14,26] The polyimide rings were confirmed by the characteristic peaks of the carbonyl groups in six-membered polyimide rings (~1670 cm^{-1} and ~1710 cm^{-1}).[14,27–30] The bands at 1331 and 1335 cm^{-1} are attributed to C–N stretching vibration peaks.[14,27,30] The bands at 1591, 1485/1501, and 1405 cm^{-1} are the C=C stretching peaks of phenyl rings. The bands at 744 and 755 cm^{-1} are the absorption peaks of C–H plane deformations of singly substituted phenyl rings.[14]

The chemical structure of DP_4A_0 and DP_4A_2 was further analyzed *via* ss ^{13}C NMR spectrometry (Fig. 2). The peaks at about 162 ppm pertained to the C=O bond in the six-membered polyimide rings.[14,27–29] The signals near 132.37/130.81 and 128.18, 122.23/122.03 ppm pertained to other aromatic carbon atoms (benzene, perylene) from the two building blocks.[14,27] The signals at 93.40/90.97 (Ar–C≡C–Ar), 82.83/83.05, and 77.87/77.64 ppm (Ar–C≡C–H) correspond to the alkynyl units in the CMPs.[14,25,31] The elemental analysis of the CMPs indicated that there is a deviation from the theoretical values, which is common for CMPs probably because of the incomplete combustion or adsorption of water and gases.[32] Fig. S1a† shows the solid UV-Vis spectra of DP_4A_0 and the corresponding building block PBr_4ABr_0. The DP_4A_0 powder shows an extra peak at 288 nm, which is not found in PBr_4ABr_0. The relative intensity of this peak decreases in the polymer. Compared to PBr_4ABr_0 with a peak at 272 nm, there is an obvious red-shift.[19] There were two strong peaks for both DP_4A_2 and PBr_4ABr_2, in which a red-shift was observed for the main peak (Fig. S1b†).[29] The results clearly indicated that products with new optical performance were formed.[28]

To ascertain the porosity of DP_4A_0 and DP_4A_2, nitrogen adsorption–desorption experiments were performed at 77 K (Fig. 3). DP_4A_0 assumes a Type I isotherm in the range of p/p_0 = 0.05–0.15 according to IUPAC classifications and then takes on a very flat adsorption plateau.[30] The gas absorption decreases sharply at lower relative pressures.[27] In sharp contrast, DP_4A_2, although similar to DP_2A_2, displays a combination of type I and type II isotherms. With the increase in the nitrogen sorption at high relative pressure, there is a palpable hysteresis phenomenon, which might be due to the existence of a mesoporous or inter-particulate void in the sample.[14] The isotherm of DP_4A_2 exhibits sharp N_2 adsorption under low relative pressure (p/p_0 < 0.01), which means that there are substantial micropores and ultra-micropores.[14,24,29,30] Using the BET model, these isotherms give apparent surface areas of 41.3 $m^2\ g^{-1}$ and 402.1 $m^2\ g^{-1}$ for DP_4A_0 and DP_4A_2, respectively (Table 1). The BET surface area of DP_4A_2, similar to that of DP_2A_2 (378 $m^2\ g^{-1}$),[14] is higher than that of DP_4A_0 although the chemical composition of DP_2A_2 and DP_4A_0 is the same. A reasonable explanation for this is the difference in the point position and degree of crosslinking.[27,29,30] The pore volumes were obtained using DFT methods from the nitrogen sorption isotherms. DP_4A_2 shows a larger total pore volume when compared

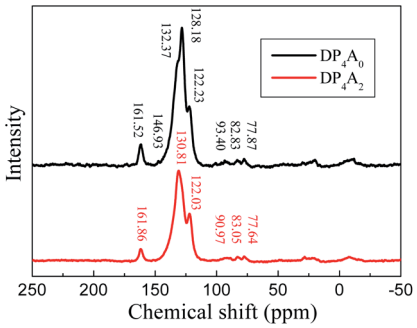

Fig. 2 The ss ^{13}C NMR spectra of DP_4A_0 and DP_4A_2.

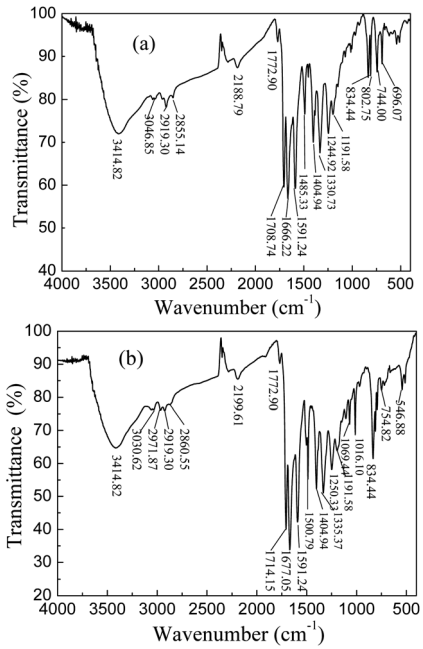

Fig. 1 FT-IR spectra of DP_4A_0 and DP_4A_2.

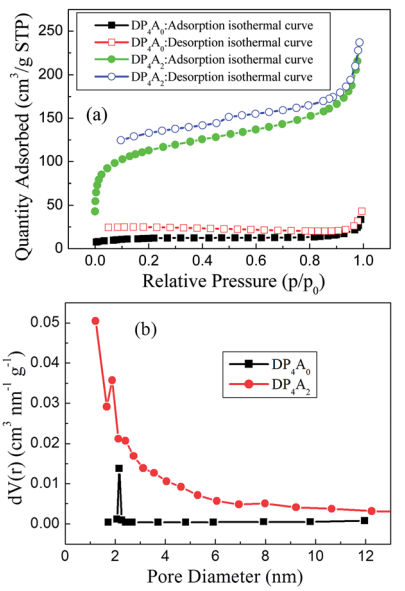

Fig. 3 (a) Nitrogen adsorption–desorption isotherms measured at 77 K for DP_4A_0 and DP_4A_2; (b) the BJH pore size distribution profiles of DP_4A_0 and DP_4A_2 calculated using the NLDFT method.

Table 1 Pore and surface properties of DP_4A_0, DP_4A_2, and DP_2A_2

CMPs	S_{BET}[a] ($m^2\ g^{-1}$)	V_{tot} (tpv)[b] ($cm^3\ g^{-1}$)	V_{micro}[c] ($cm^3\ g^{-1}$)	V_{micro}/V_{tot}	S_{micro}[c] ($m^2\ g^{-1}$)	$S_{external}$[c] ($m^2\ g^{-1}$)
DP_4A_0	41.3	0.03772	0.00743	0.1971	16.9	24.4
DP_4A_2	402.1	0.3665	0.2319	0.6327	115.9	170.4
DP_2A_2	378.0	0.2804	0.1008	0.3595	217.8	160.2

[a] Specific surface area calculated from the adsorption branch of the nitrogen isotherm using the BET method with a relative pressure (p/p_0) range from 0.01 to 0.10. [b] The total pore volume was obtained from the BET data up to $p/p_0 = 0.99$ and is defined as the sum of the micropore volume and the volumes of larger pores. [c] The micropore volume was calculated from the nitrogen adsorption isotherm using the *t*-plot method.

to DP_4A_0 and is similar to DP_2A_2 (Table 1). The ratio of V_{mic}/V_{tot} can be used as a scale for the degree of microporosity in the CMPs. DP_4A_2 shows a high degree of microporosity, of which 63.27% of the total pore volume consists of micropores. The low volume ratio of DP_4A_0 indicates clearly that there is a certain amount of large pores or interparticulate porosity.[29,30] The degree of crosslinking in DP_4A_2 is 6, which is larger than that of DP_4A_0 and DP_2A_2 (4); therefore, DP_4A_2 has a higher specific surface area and microporosity compared to DP_4A_0 and DP_2A_2. Although the crosslinking degree of both DP_4A_0 and DP_2A_2 is 4, their crosslinking point position is different. The positions of the crosslinking points in DP_4A_0 are located at the 1, 6, 7, and 12 positions, while that of DP_2A_2 are located at the 1,7,13, and 14 positions. Because the positions of the crosslinking points in DP_4A_0 are more crowded than that of DP_2A_2, thus the specific surface area and microporosity of DP_4A_0 are much lower than that of DP_2A_2. The pore volume distributions as a function of the pore width for DP_4A_0 and DP_4A_2 were estimated *via* the nonlocal DFT (NLDFT) method (Fig. 3b). It can be seen that DP_4A_0 possesses a narrow pore size distribution in the minor region with a pore size centered at 2.15 nm. DP_4A_0 has a very low total pore volume and there are both micropores and pores in the mesopore region.[27,29] The N_2 sorption isotherm of DP_4A_2 indicated that DP_4A_2 includes a certain amount of pores with a relatively broad diameter distribution from 1 to 4 nm and a large proportion of the pores are centered at 1.22 nm. Although micropores dominate in DP_4A_2, there is a certain proportion of mesopores in the DP_4A_2 network.[14,27]

DP_4A_0 and DP_4A_2 are all black powders. They are not soluble in water and common organic solvents and are also chemically stable in dilute aqueous solutions of acids or bases due to their highly crosslinked structures. There are a few weight losses at 275 and 362 °C due to escaping solvent that was caught inside the polymer networks. They have excellent thermal stability with decomposition temperatures (T_{dec}) of 453 and 547 °C determined at 5% mass loss and char yields of 60.01% and 90.26% at 800 °C under a N_2 atmosphere (Fig. 4). The high thermal stability is due to the covalent bonds, the high crosslinking density of the networks, and the good stability of the perylene imide backbones.[14,27–30] PXRD measurements confirmed the amorphous feature of the CMPs (Fig. S2†),[27,30] which are expected for a typical non-dynamic covalently crosslinked CMP materials.[33] Morphologies monitored by SEM demonstrate that DP_4A_0 displays a *Tremella fuciformis*-like morphology.[30] DP_4A_2 exhibits a floppy surface and an interconnected spherical particle-like morphology (Fig. 5).[27–29]

We investigated the emission spectra of DP_4A_0 and DP_4A_2 in different polar solvents (Fig. 6), including ACN, DMF, acetone, THF, chloroform, DOX, and EtOH.[3,4,34] It was found that DP_4A_0 and DP_4A_2 disperse liquid in DMF, DOX, chloroform, and THF and exhibited purple or yellow emission when excited with 365 nm UV light.[6,35,36] Thanks to the completely π-conjugated skeleton from the connection of the phenyl rings, DP_4A_0 and DP_4A_2 exhibited the strongest fluorescence in THF (λ_{ex} = 370 nm) and DOX (λ_{ex} = 365 nm) suspensions, respectively.[22,35,36] Their ability to use fluorescence sensing to detect NACs (such as *o*-NP) was discussed. As shown in Fig. S3,† a rapid and clearly visible fluorescence turn-off response was observed upon increasing the concentration of *o*-NP in the solution. As the concentration of *o*-NP in the solution increased, a fast fluorescence turn-off response occurred, which signified that DP_4A_0 and DP_4A_2 enable effective "real-time" detection of *o*-NP.[4,37]

We investigated DP_4A_0 and DP_4A_2 as fluorescent probes for sensing NACs by successively adding NACs, such as NB, PA, DNT, *p*-DNB, *o*-NP, p-NT, *m*-DNB, and non-nitroaromatic analytes including PhOH. Fig. 7 and S4–S6† show the fluorescence spectra and I_0/I plots of DP_4A_0 and DP_4A_2 before and after adding NACs and different degrees of quenching were observed after the addition of the NACs. The fluorescence of DP_4A_0 and DP_4A_2 was almost completely quenched after the addition of *o*-NP, while the fluorescence was not obviously quenched after the addition of other NACs (PA, NB, DNT, *p*-NT, *p*-DNB, *m*-DNB, and PhOH), indicating that DP_4A_0 and DP_4A_2 exhibit extremely high selectivity for *o*-NP.[37,38] Furthermore, the fluorescence intensity of DP_4A_0 and DP_4A_2 were overwhelmingly affected by the molar concentration of *o*-NP. To qualitatively comprehend the

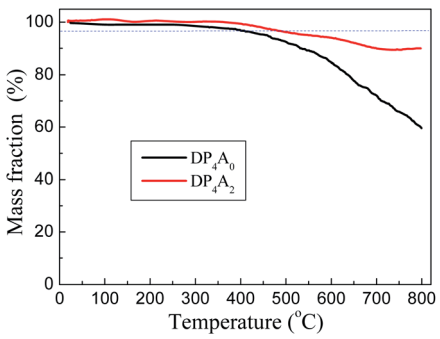

Fig. 4 TGA thermograms of DP_4A_0 (black) and DP_4A_2 (red), measured in a nitrogen atmosphere at a heating rate of 10 °C min^{-1}.

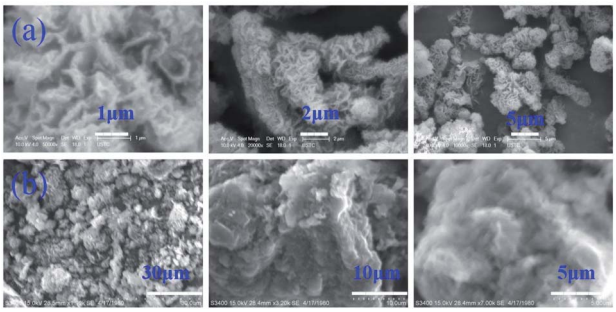

Fig. 5 SEM images of (a) DP_4A_0 and (b) DP_4A_2.

quenching influence of *o*-NP on DP_4A_0 and DP_4A_2, the quenching coefficients (K_{sv}) were calculated using the Stern–Volmer (S–V) equation: $I_0/I = 1 + K_{sv}[Q]$ (I_0 and I are the fluorescent intensities of DP_4A_0 or DP_4A_2 before and after the addition of the analyte and [Q] is the concentration of the analyte). As shown in Fig. 7c, good linear S–V relationships were observed for DP_4A_0 and DP_4A_2, and the K_{sv} were up to 4 orders of magnitude greater than before the addition of *o*-NP, which indicated that DP_4A_0 and DP_4A_2 have high sensitivity to *o*-NP.[5,23,34,38,39] In addition, the LODs of DP_4A_0 and DP_4A_2 to *o*-NP are 5.73×10^{-9} and 7.36×10^{-9} mol L^{-1}, respectively, also indicating a high sensitivity to *o*-NP.[4–6] Fig. 8 shows that as more *o*-NP was added, the tighter the aggregates of both CMPs were, meaning that there are intense interactions between both CMPs and *o*-NP.[14,40,41]

Again it can be seen from Tables 2 and S1† that the sensitivity to *o*-NP is ordered DP_2A_2 > DP_4A_0 > DP_4A_2. There are similar trends for the sensitivity to PA and DNT.[14] We speculated that the former is caused by the different positions of the crosslinking points, and the latter is caused by the excessive crosslinking density, which limits the conjugation effects of DP_4A_2. Since the crosslinking density of DP_4A_2 (6) is greater than that of DP_2A_2 and DP_4A_0 (4), the degree of conjugation in the DP_4A_2 network is lower than that of DP_2A_2 and DP_4A_0, which is not conducive to the transfer of electrons. Therefore, although the specific surface area, pore volume, and micropore volume of DP_4A_2 are larger than that of DP_2A_2 and DP_4A_0, the sensitivity of DP_4A_2 to *o*-NP is lower than that of DP_2A_2 and DP_4A_0. The crosslinking density of DP_4A_0 and DP_2A_2 is the same but the positions of the crosslinking points are different.

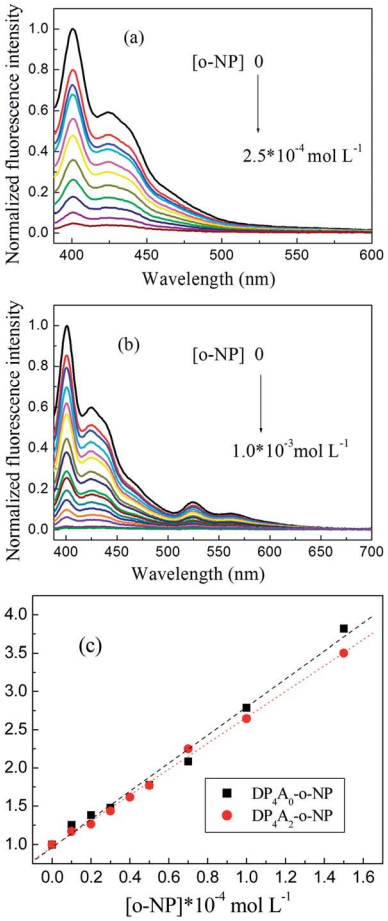

Fig. 7 The changes in fluorescence spectra of (a) DP_4A_0 and (b) DP_4A_2 dispersions in THF and DOX upon the addition of *o*-NP; (c) S–V plots of DP_4A_0 and DP_4A_2 with various concentrations of *o*-NP (1.0 mg mL^{-1}, excited at 370 and 365 nm).

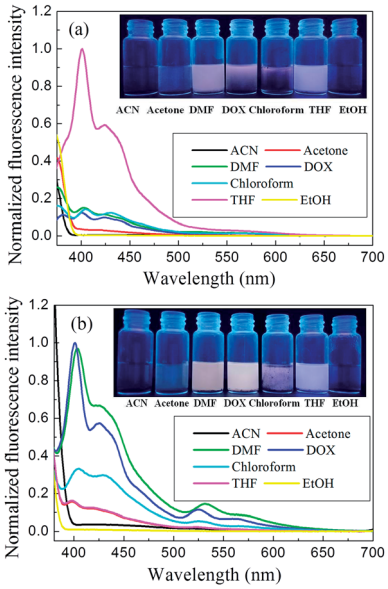

Fig. 6 Fluorescent emission spectra of (a) DP_4A_0 (λ_{ex} = 370 nm) and (b) DP_4A_2 (λ_{ex} = 365 nm) dispersed in various solvents. Insets: photographs of solvent dispersed DP_4A_0 and DP_4A_2 excited with UV light at 365 nm.

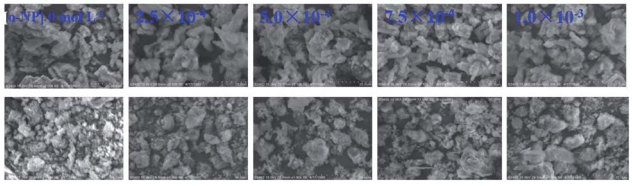

Fig. 8 The SEM images of (a) DP_4A_0 (top) and (b) DP_4A_2 (bottom) in the absence and presence of *o*-NP at various concentrations.

Table 2 The equations of I_0/I for DP_4A_0, DP_4A_2, and DP_2A_2 with the concentration of *o*-NP, suspended in THF and DOX with excitation at 370 and 365 nm

CMPs	The equation	Regression coefficient (R)	Concentration range of NACs (mol L^{-1})	Limits of detection (mol L^{-1})
DP_4A_0	$I_0/I = 0.962 + 1.83 \times 10^4$ [*o*-NP]	0.9948	0 to 1.5×10^{-5}	5.73×10^{-9}
DP_4A_2	$I_0/I = 0.966 + 1.69 \times 10^4$ [*o*-NP]	0.9983	0 to 1.5×10^{-4}	7.36×10^{-9}
DP_2A_2	$I_0/I = 1.001 + 1.998 \times 10^4$ [*o*-NP]	0.9924	0 to 3.5×10^{-5}	1.50×10^{-9}

Because the position of crosslinking points in DP_4A_0 is closer than that of DP_2A_2, the conjugate property of DP_4A_0 is lower than that of DP_2A_2. Moreover, the specific surface area and micropore properties of DP_4A_0 are much lower than that of DP_2A_2 and the chance of contact between the active sites of DP_4A_0 and *o*-NP is less than that of DP_2A_2, thus the sensitivity of DP_4A_0 to *o*-NP is lower than that of DP_2A_2.

To investigate the cross-effects of other NACs, we also conducted competitive experiments to further explore the selectivity of DP_4A_0 and DP_4A_2 to *o*-NP. The I_0/I values of DP_4A_0 and DP_4A_2 in different NACs mixtures with and without *o*-NP are recorded in Fig. 9. After adding other NACs (*e.g.* NB, *m*-DNB, *p*-DNB, *p*-NT, DNT, and phenol), the I_0/I values for DP_4A_0 or DP_4A_2 did not change significantly, with the exception of the PA experiment. When PA was added to a solution of DP_4A_0 or DP_4A_2 containing *o*-NP, the I_0/I value increased significantly. There are signs that DP_4A_0 and DP_4A_2 have unusually high selectivity to *o*-NP.[4,5]

At higher concentrations of NACs the shapes of the curves are due to a superamplified quenching effect.[42] As shown in Fig. S5,† the S–V plots exhibited hyperbolic curves, which suggests that they are both static and dynamic quenching phenomena occurring at the same time in the detecting process.[4,39,43]

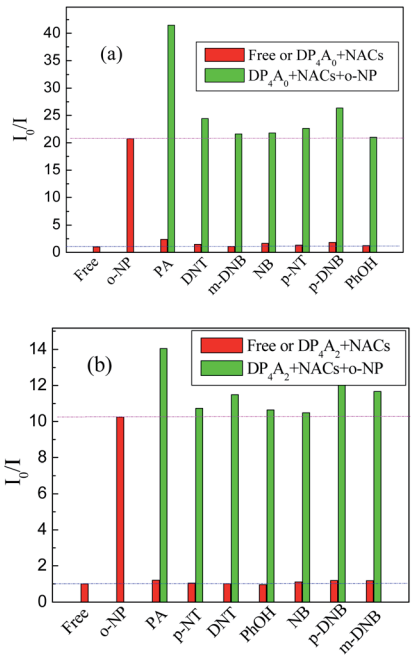

Fig. 9 The selectivity and competitiveness of DP_4A_0 and DP_4A_2 (1.0 mg mL^{-1}) for sensing NACs at the same concentration of 2.5×10^{-4} mol L^{-1} of *o*-NP in THF and DOX (λ_{ex} = 370 and 365 nm).

Fluorescence resonance energy transfer (FRET) and photo-induced electron transfer (PET) mechanisms were explored to understand the sensing performance of DP_4A_0 and DP_4A_2. The absorption spectra of the NACs have almost no overlap with the emission spectra of DP_4A_0 (besides *p*-NT, *m*-DNB) and DP_4A_2 (except for *o*-NP, PA), indicating that the fluorescence quenching mainly resulted from PET process between electron-rich DP_4A_0 or DP_4A_2 and the electron deficient NACs (Fig. S7†).[34,44–47] In order to assess the feasibility of PET from DP_4A_2 and DP_4A_2 to NACs, the lowest-unoccupied molecular orbital (LUMOs) energy levels and the highest occupied molecular orbital (HOMO) energy levels of DP_4A_0 and DP_4A_2 were calculated.[34] As shown in Fig. S8 and Table S2,† the LUMO levels of DP_4A_0 and DP_4A_2 are higher than that of the NACs, which allows for electron transfer from DP_4A_0 and DP_4A_2 to the NACs.[4] For example, the LUMO energy levels of PA and *p*-DNB are lower than that of DP_4A_0 and DP_4A_2.[34,48] However, the LUMO levels are not the only factor affecting the PET process, it is also necessary to take into account the HOMO energy level of the NACs if it is lower than that of the CMPs. Hence, although the LUMO energies of DP_4A_0 and DP_4A_2 are lower than that of NB, DNT, *p*-NT, *m*-DNB, *o*-NP, and PhOH, a PET process can occur as well.[34,49] Generally speaking, nitro groups play an important part in fluorescence quenching because their contribution to the LUMO energies is achieved by utilizing their electron withdrawing ability. Therefore, with increasing numbers of nitro groups, lower LUMO energy levels are obtained, thus improving electron transfer efficiency.[6,39] The interaction of the analytes with DP_4A_0 and DP_4A_2, as well as efficient PET are considered the key parameters in the quenching mechanism.

However, the fluorescence quenching phenomena cannot exclude the possibility of a FRET mechanism. O–H$\cdots\pi$ and OH$\cdots$N interactions may also impact the sensitivity of DP_4A_0 and DP_4A_2 for detecting *o*-NP.[39] The NAC-containing hydroxyl groups (PA, NP, and PhOH) can effectively cause fluorescence quenching. This may be due to weak interactions such as hydrogen bonding of hydroxyl groups with nitrogen, oxygen, and π-electrons in the framework.[39,50,51] The results indicated that there are three important factors for the detection of NACs, *i.e.*, nitro groups, hydrogen bonding, and N, O$\cdots\pi$ interactions (Fig. S9†).[6] High quenching constants and quenching rates, together with extremely low LOD values, make DP_4A_0 and DP_4A_2

highly sensitive chemical sensors for detecting NACs, particularly *o*-NP.[39]

In order to study the fluorescence stability of DP_4A_0 and DP_4A_2, annealing experiments were carried out. Solid powders of DP_4A_0 and DP_4A_2 were heated to 50 °C for half an hour in the atmosphere. Then, the temperature was increased to 100 °C where it was maintained for another half an hour. The temperature was then increased to 150 °C and 200 °C. After cooling, the samples were scattered in DOX or THF at a polymer concentration of 1.0 mg mL^{-1}. Fig. S10† shows the fluorescence spectra of DP_4A_0 and DP_4A_2 after annealing in the atmosphere. As can be seen that they were still quite stable after heating to 100 °C for half an hour, and the fluorescence spectra were nearly the same as before heating. As the temperature increased, the fluorescence peak intensities decreased but there was no red-shift observed. Below 100 °C, fluorescence emission is stable. This result is due to the chemical structures of DP_4A_0 and DP_4A_2 and their stable perylene units.[14,52,53]

Conclusions

In summary, we have succeeded in developing solvent dispersible, fluorescent conjugated microporous polymers by taking advantage of Sonogashira–Hagihara cross-coupling reactions. We employed these systems as chemosensors for sensing nitroaromatic compounds. The two CMPs exhibit high BET specific surface areas and total pore volumes. They emitted strong purple and yellow fluorescence under UV light. It was found that DP_4A_0 dispersion in THF and DP_4A_2 dispersion in DOX can be effectively utilized to detect *o*-NP by fluorescence quenching in real-time. Specifically, DP_4A_0 and DP_4A_2 exhibited high selectivity to *o*-NP over other NACs. The relationship between the fluorescence intensity and *o*-NP concentration can be quantified. The detection limits of *o*-NP using DP_4A_0 and DP_4A_2 as probes were estimated to be 5.73×10^{-9} and 7.36×10^{-9} mol L^{-1}. The possible fluorescence sensing mechanism of both CMPs was deemed to be an electron transfer as well as hydrogen bonding and N, O$\cdots\pi$ interactions. The sensing performance of DP_4A_0 and DP_4A_2 was dependent on the position of the crosslinking points and crosslinking density.

Conflicts of interest

There are no conflicts to declare.

Acknowledgements

This work was supported by the Natural Science Foundation of the Anhui Education Department (under Grant No. KJ2018A0319).

Notes and references

1 Y. Salinas, R. Martınez-Manez, M. D. Marcos, F. Sancenon, A. M. Costero, M. Parra and S. Gil, *Chem. Soc. Rev.*, 2012, **41**, 1261–1296.
2 X. Sun, Y. Wang and Y. Lei, *Chem. Soc. Rev.*, 2015, **44**, 8019–8061.
3 V. S. Mothika, A. Räupke, K. O. Brinkmann, T. Riedl, G. Brunklaus and U. Scherf, *ACS Appl. Nano Mater.*, 2018, **11**, 6483–6492.
4 N. Jiang, G. Li, W. Che, D. Zhu, Z. Su and M. R. Bryce, *J. Mater. Chem. C*, 2018, **41**, 11162–11169.
5 M. Wang, H. Zhang, L. Guo and D. Cao, *Sens. Actuators, B*, 2018, **274**, 102–109.
6 R. Sun, X. Huo, H. Lu, S. Feng, D. Wang and H. Liu, *Sens. Actuators, B*, 2018, **265**, 476–487.
7 K. M. Roscioli, E. Davis, W. F. Siems, A. Mariano, W. Su, S. K. Guharay and H. H. Hill, *Anal. Chem.*, 2011, **83**, 5965–5971.
8 H. Ma, F. Li, P. Li, H. Wang, M. Zhang, G. Zhang, M. Baumgarten and K. Müllen, *Adv. Funct. Mater.*, 2016, **26**, 2025–2031.
9 C. Gu, N. Huang, Y. Wu, H. Xu and D. Jiang, *Angew. Chem., Int. Ed.*, 2015, **54**, 11540–115404.
10 M. Martin, M. Crain, K. Walsh, R. A. Mcgill, E. Houser, J. Stepnowski, S. Stepnowski, H. D. Wu and S. Ross, *Sens. Actuators, B*, 2007, **126**, 447–454.
11 M. Rahimi-Nasrabadi, M. M. Zahedi, S. M. Pourmortazavi, R. Heydari, H. Rai, J. Jazayeri and A. Javidan, *Microchim. Acta*, 2012, **177**, 145–152.
12 J. M. Sylvia, J. A. Janni, J. D. Klein and K. M. Spencer, *Anal. Chem.*, 2000, **72**, 5834–5840.
13 Y. K. Li, S. M. Bi, F. Liu, S. Y. Wu, J. Hu, L. M. Wang, H. L. Liu and Y. Hu, *J. Mater. Chem. C*, 2015, **3**, 6876–6881.
14 T. M. Geng, D. K. Li, Z. M. Zhu, W. Y. Zhang, S. N. Ye, H. Zhu and Z. Q. Wang, *Anal. Chim. Acta*, 2018, **1011**, 77–85.
15 J. S. Yang and T. M. Swager, *J. Am. Chem. Soc.*, 1998, **120**, 11864.
16 W. Huang, M. Bender, K. Seehafer, I. Wacker, R. R. Schröder and U. H. F. A. Bunz, *Macromolecules*, 2018, **51**, 1345–1350.
17 Y. Xu, S. Jin, H. Xu, A. Nagai and D. Jiang, *Chem. Soc. Rev.*, 2013, **42**, 8012–8031.
18 J. X. Jiang, F. B. Su, A. F. Trewin, C. D. Wood, N. L. Campbell, H. Niu, C. Dickinson, A. Y. Ganin, M. J. Rosseinsky, Y. Z. Khimyak and A. I. Cooper, *Angew. Chem., Int. Ed.*, 2007, **46**, 8574–8578.
19 B. Bonillo, R. S. Sprick and A. I. Cooper, *Chem. Mater.*, 2016, **10**, 3469–3480.
20 X. Li, Z. Li and Y. W. Yang, *Adv. Mater.*, 2018, **30**, 1800177.
21 L. Sun, Y. Zou, Z. Liang, J. Yu and R. Xu, *Polym. Chem.*, 2014, **5**, 471–478.
22 S. Wang, Y. Liu, Y. Yu, J. Du, Y. Cui, X. Song and Z. Liang, *New J. Chem.*, 2018, **42**, 9482–9487.
23 W. Donga, Z. Ma, Q. Duan and T. Fei, *Dyes Pigm.*, 2018, **159**, 128–134.
24 M. C. Baier, J. Huber and S. Mecking, *J. Am. Chem. Soc.*, 2009, **131**, 14267–14273.
25 P. Wang, H. L. Zhang and L. Zhang, *Chem. Ind. Eng. Prog.*, 2000, **3**, 460–463.
26 S. J. Ren, R. Dawson, D. J. Adams and A. I. Cooper, *Polym. Chem.*, 2013, **4**, 5585–5590.
27 M. R. Liebl and J. Senker, *Chem. Mater.*, 2013, **25**, 970–980.

28 Y. Liao, J. Weber and C. F. J. Fau, *Macromolecules*, 2015, **48**, 2064–2073.
29 K. V. Rao, R. Haldar, C. Kulkarni, T. K. Maji and S. J. Georg, *Chem. Mater.*, 2012, **24**, 969–971.
30 S. Wu, S. Gu, A. Zhang, G. Yu, Z. Wang, J. Jian and C. Pan, *J. Mater. Chem. A*, 2015, **3**, 878–885.
31 L. Chen, Y. Honsho, S. Seki and D. L. Jiang, *J. Am. Chem. Soc.*, 2010, **132**, 6742–6748.
32 X. Y. Wang, C. Zhang, Y. Zhao, S. J. Ren and J. X. Jiang, *Macromol. Rapid Commun.*, 2016, **37**, 323–329.
33 S. Bhunia, N. Dey, A. Pradhana and S. Bhattacharya, *Chem. Commun.*, 2018, **54**, 7495–7498.
34 F. Wei, X. Cai, J. Nie, F. Wang, C. Lu, G. Yang, Z. Chen, C. Ma and Y. Zhang, *Polym. Chem.*, 2018, **27**, 3832–3839.
35 A. Mal, R. K. Mishra, V. K. Praveen, M. A. Khayum, R. Banerjee and A. Ajayaghosh, *Angew. Chem.*, 2018, **57**, 8579–8583.
36 Y. Yang, L. Feng, J. Ren, Y. Liu, S. Jin, L. Su, C. Wood and B. Tan, *Macromol. Rapid Commun.*, 2018, **1**, 1800441.
37 X. Liu, Y. Xu and D. Jiang, *J. Am. Chem. Soc.*, 2012, **134**, 8738–8741.
38 M. W. Zhu, S. Q. Xu, X. Z. Wang, Y. Chen, L. Dai and X. Zhao, *Chem. Commun.*, 2018, **54**, 2308–2311.
39 K. Saumya and S. C. Veettil, *J. Photochem. Photobiol., A*, 2019, **371**, 414–422.
40 N. Niamsa, C. Kaewtong, W. Srinonmuang, B. Wanno, B. Pulpokab and T. Tuntulani, *Polym. Chem.*, 2013, **4**, 3039–3046.
41 Y. D. Hang, J. Wang, T. Jiang, N. N. Lu and J. L. Hua, *Anal. Chem.*, 2016, **88**, 1696–1703.
42 J. Liu, Y. Zhong, P. Lu, Y. Hong, J. W. Y. Lam, M. Faisal, Y. Yu, K. S. Won and B. Z. Tang, *Polym. Chem.*, 2010, **1**, 426–429.
43 X. G. Hou, Y. Wu, H. T. Cao, H. Z. Sun, H. B. Li, G. G. Shan and Z. M. Su, *Chem. Commun.*, 2014, **50**, 6031–6034.
44 N. Sang, C. X. Zhan and D. P. Cao, *J. Mater. Chem. A*, 2015, **3**, 92–96.
45 L. Guo, M. Wang, X. Zeng and D. Cao, *Mater. Chem. Front.*, 2017, **1**, 2643–2650.
46 T. M. Geng, S. N. Ye, Y. Wang, H. Zhu, X. Wang and X. Liu, *Talanta*, 2017, **165**, 282–288.
47 S. Pramanik, C. Zheng, X. Zhang, T. J. Emge and J. Li, *J. Am. Chem. Soc.*, 2011, **133**, 4153–4155.
48 X. J. Qi, Y. H. Jin, N. Li, Z. Wang, K. C. Wang and Q. H. Zhang, *Chem. Commun.*, 2017, **53**, 10318–10321.
49 C. L. Zhang, S. M. Zhang, Y. H. Yan, F. Xia, A. N. Huang and Y. H. Xian, *ACS Appl. Mater. Interfaces*, 2017, **9**, 13415–13421.
50 S. Dalapati, S. Jin, J. Gao, Y. Xu, A. Nagai and D. Jiang, *J. Am. Chem. Soc.*, 2013, **135**, 17310–17313.
51 S. J. Toal and W. C. Trogler, *J. Mater. Chem.*, 2006, **16**, 2871–2883.
52 G. He, H. Peng, T. Liu, M. Yang, Y. Zhang and Y. Fang, *J. Mater. Chem.*, 2009, **19**, 7347–7453.
53 W. B. Wu, S. H. Ye, G. Yu, Y. Q. Liu, J. G. Qin and Z. Li, *Macromol. Rapid Commun.*, 2012, **33**, 164–171.